ARTICLE

Optimising Thermochemical Energy Storage: A Comprehensive Analysis of $CaCO_3$ composites with $CaSiO_3$, $CaTiO_3$, and $CaZrO_3$†

Received 00th January 20xx,
Accepted 00th January 20xx

DOI: 10.1039/x0xx00000x

Terry D. Humphries,*[a] Adriana P. Vieira,[a] Yurong Liu,[a] Eleanor McCabe,[a] Mark Paskevicius [a] and Craig E. Buckley [a]

With the increasing amount of renewable energy produced, many governments and industries are pushing for the installation of battery energy storage system (BESS) solutions. Thermal batteries are systems that store heat made from various energy sources, and can be used to produce electricity upon demand. These systems are easily scalable and can be installed in cities, homes and remote locations. Thermochemical energy storage (TCES) uses the enthalpy of a chemical reaction to store and release heat through endothermic and exothermic processes, respectively. $CaCO_3$ has been identified as an ideal TCES material as it is cheap and abundant, but maximising long-term cyclability is key to ensure battery longevity. This article investigates the addition of $CaSiO_3$, $CaTiO_3$ and $CaZrO_3$ to $CaCO_3$ in a 1:1 ratio to ascertain the reaction properties and cyclic capacity over time. Cycling longevity and thermodynamic properties were determined using simultaneous differential scanning calorimetry and thermogravimetric analysis (DSC-TGA) along with the Sieverts technique, and their reaction pathway studied by powder X-ray diffraction (XRD) and scanning electron microscopy (SEM). The low cost of the $CaCO_3$-$CaSiO_3$ material of \$1.8 USD/kWh_{th} suggests that if a suitable particle refinement agent were to be employed to ensure cycling longevity this material would be an excellent TCES material. Despite the CO_2 cycling capacity of the $CaCO_3$-$CaZrO_3$ system only reducing by 16 wt.% over 100 cycles, the cost of ZrO_2 brings the materials cost to \$30.9 USD/kWh_{th}, making this material currently unsuitable for application. The $CaCO_3$-$CaTiO_3$ system showed only a 17 % drop in total CO_2 uptake over 100 cycles, although the cost was \$11.1 USD/kWh_{th}.

Introduction

Solar energy is considered to be one of the most promising renewable resources; however, the main restriction in its application is the disparity between supply and demand.[1] Concentrated solar power (CSP) plants have the potential to be integrated into the grid for power generation, but power production is unstable in CSP plants due to intermittent solar energy.[2] It is necessary to integrate stable and economically feasible thermal energy storage systems (TES) that can store heat during solar exposure and release heat when there is no solar irradiation.[3-5] The integration of a TES with CSP is an efficient and sustainable solution to the use of solar energy.[4, 6] Sensible heat storage (SHS) is used in current generation TES systems commercially available for CSP, which use molten salts ($NaNO_3$-KNO_3) to store heat through their specific heat capacity. Despite their commercial viability, molten salts present some issues such as low energy density, which requires massive storage volumes and material quantities at moderate cost, and they also have issues with corrosion of containment vessels.[7]

Thermochemical energy storage (TCES) systems are an emerging form of TES based on reversible thermochemical reactions, often between a solid and a gas.[4, 6, 8, 9] An endothermic chemical reaction absorbs thermal energy, charging the thermal battery at times of high solar irradiance. The energy is stored until required and is released by an exothermic chemical reaction (thermal battery discharge) at times of low solar irradiance. Among the materials investigated for TCES, metal carbonates,[4, 9] metal hydrides,[11–14] metal oxides[4] and metal hydroxides[5] have been emphasised due to their reversible gas-solid reactions, abundance, low cost, high operation temperatures, and noncorrosive nature.

$SrCO_3$ and $BaCO_3$ have been presented as materials for TCES systems,[4, 10-13] however, researchers highlight that $CaCO_3$ is also a promising candidate due to its low cost and high energy density.[4, 14-17] The main drawback in terms of using $CaCO_3$ in TCES applications is the degradation of the material over multiple cycles of energy storage and release. This loss in cycling capacity is due to powder sintering at high temperatures, which results in a reduction in the amount of CaO that can be carbonated in each thermal release cycle.[4] Fortunately, the use of additives such as aluminium oxide has been shown to overcome this issue and result in a prolonged cycle life of the $CaCO_3$ TCES system.[4, 14, 17] The desired operating temperature for the next generation of TCES for CSP applications is between 700 and 1100 °C.[18] Although, $CaCO_3$ can operate at 900 °C, lower

[a] Physics and Astronomy, Institute for Energy Transitions, Curtin University, GPO Box U1987, Perth, WA 6845, Australia.
* Corresponding author: terry_humphries81@hotmail.com
† Electronic Supplementary Information (ESI) available.
See DOI: 10.1039/x0xx00000x

temperatures closer to 700 °C will be more technically feasible from an engineering perspective for a full scale system.[4]

Reactive carbonate composites (RCC), which use the combination of a metal carbonate and an additive, such as $SrCO_3$-$SrSiO_3$, $SrCO_3$-$SrTiO_3$, $BaCO_3$-$BaSiO_3$ and $BaCO_3$-Fe_3O_4 were demonstrated to be effective ways to tune the thermodynamics of CO_2 release and absorption.[10-13] This provides a method of changing the temperature and pressure at which the thermochemical reaction occurs. Based on this information, the present study shows the experimental investigation of the thermal energy storage properties of the $CaCO_3$-$CaSiO_3$ RCC for which thermodynamic predictions show that the addition of $CaSiO_3$ will lower the operating temperature of the $CaCO_3$ system to 556 °C instead of 886 °C under 1 bar CO_2 with $\Delta H_{556°C}$ = 121.3 kJ/mol and $\Delta S_{556°C}$ = 146.3 J/mol.[19] At the same time, $CaTiO_3$ or $CaZrO_3$ have individually been added to $CaCO_3$ (eqn 2) to determine whether the cyclic absorption of CO_2 can be improved by inhibition of particle agglomeration. The cyclability of these three systems has been examined by simultaneous differential scanning calorimetry and thermogravimetric analysis (DSC-TGA) and their reaction pathway studied by powder X-Ray Diffraction (XRD) and Scanning Electron Microscopy (SEM). Lastly, a cost analysis was performed to determine the feasibility of these materials for use in thermal batteries.

$$CaCO_{3(s)} + CaSiO_{3(s)} \rightleftharpoons Ca_2SiO_{4(s)} + CO_{2(g)} \quad (1)$$

$$CaCO_{3(s)} + CaMO_{3(s)} \rightleftharpoons CaO + CaMO_{3(s)} + CO_{2(g)} \, (M = \text{Ti, Zr}) \quad (2)$$

Experimental

All powders were purchased from Sigma-Aldrich and used as received: calcium carbonate, $CaCO_3$ (≥ 99.0%), silicon dioxide, SiO_2 (99.5%), zirconium dioxide, ZrO_2 (99.6%) and titanium dioxide, TiO_2 (99.8%).

Calcium metasilicate ($CaSiO_3$), calcium titanate ($CaTiO_3$) and calcium zirconate ($CaZrO_3$) were prepared by solid-state reaction using a method previously described (eq. 3).[20] $CaCO_3$ and SiO_2 were pre-heated separately for 3 h at a temperature of 600 °C in air to remove moisture. A 1:1.1 molar mixture ($CaCO_3$: SiO_2) was ball-milled for 16 hours (60 min milling and 1 min break, repeated 16 times), in 316 stainless steel milling vials (80 mL) with 316 stainless steel balls (10 mm diameter) using an Across International Planetary Ball Mill (PQ-N04) with a ball-to-powder mass ratio of 10:1. The mixture was then heated in air at a rate of 20 °C min^{-1} from room temperature to 1000 °C, before being kept isothermal for 3 h and then cooled to room temperature. Similar procedures were performed to synthesise $CaTiO_3$ and $CaZrO_3$ using mixtures of $CaCO_3$-TiO_2, and $CaCO_3$-ZrO_2, respectively.

$$CaCO_{3(s)} + MO_{2(s)} \rightarrow CaMO_{3(s)} + CO_{2(g)} \, (M = \text{Si, Ti, Zr}) \quad (3)$$

The RCC's were prepared by ball milling $CaCO_3$ with either $CaSiO_3$, $CaTiO_3$ or $CaZrO_3$ (molar ratio 1:1) for 1 hour (20 min milling, one minute break, repeated three times, ball-to-powder mass ratio of 10:1). The samples obtained were designated as $CaCO_3$-$CaSiO_3$, $CaCO_3$-$CaTiO_3$, and $CaCO_3$-$CaZrO_3$, respectively. Samples of $CaCO_3$ measured without additives were not ball milled.

Powder X-ray diffraction (XRD) data were collected on a Bruker D8 Advance equipped with a Cu X-ray source (Cu $K\alpha_{1,2}$ radiation) in flat-plate Bragg–Brentano geometry. Data were collected in the 2Θ range 5 – 80° using a Lynxeye PSD detector. The diffraction patterns were quantitatively analysed with the Rietveld method using TOPAS (Bruker-AXS).[21]

Differential scanning calorimetry and thermogravimetric analysis (DSC-TGA) were performed simultaneously on a Netzsch STA 449 F3 Jupiter instrument equipped with a Pt furnace. All samples were measured inside Al_2O_3 crucibles with lids that possess a pinhole to allow gas release. The temperature and sensitivity of the DSC was calibrated using reference materials In, Zn, Al, Ag, and Au, resulting in a temperature accuracy of ± 0.2 °C, while the balance has a precision of ± 20 µg. DSC-TGA samples (~ 10 mg) were heated at a rate of 10 °C min^{-1} from room temperature to 1200 °C, under an inert atmosphere (Ar 40 mL min^{-1}) to ensure full decomposition had occurred and assess if any other phase changes occur after decomposition. To determine the operational temperature for the desorption and absorption cycles of CO_2, initial TGA CO_2 sorption tests were conducted. The samples (~ 10 mg) were first heated at 20 °C min^{-1} under an inert atmosphere (Ar 40 mL min^{-1}) up to 900 °C. The samples were kept isothermal for 5 minutes before cooling to 500 °C at 10 °C min^{-1} before another 10 min isothermal step. The samples were then heated at 20 °C min^{-1} in a CO_2-rich atmosphere (CO_2 80 mL min^{-1}, Ar 20 mL min^{-1}, 0.8 bar CO_2 partial pressure) up to 1000 °C, kept constant for 20 min and then cooled to 500 °C at 10°C/min. For the CO_2 cycling studies, ~ 10 mg of sample was heated at a rate of 20 °C min^{-1} from room temperature to 750 °C, under an inert atmosphere (Ar 40 mL min^{-1}) to promote full CO_2 desorption. The temperature was then kept isothermal at 750 °C and the gas flow was changed to 100 mL min^{-1} of CO_2 and 20 mL min^{-1} of Ar to absorb CO_2 (0.83 bar CO_2 partial pressure). After 60 min, the atmosphere was switched again to Ar 40 mL min^{-1} for 15 min to promote desorption. This process was repeated several times according to the performance of each material. The CO_2 conversion ratio (χ) was calculated using equation (4):

$$\chi = \frac{(w_t - w_i)}{w_i} \times \frac{M_f}{M_{CO_2}} \quad (4)$$

Where w_t and w_i are the weight of the sample at time t and after full CO_2 desorption, respectively. M_f and M_{CO_2} are the molar mass of the material after CO_2 desorption and CO_2 molar mass, respectively.

CO_2 cycling measurements and Pressure-Composition-Isotherms (PCI) were also measured with a computer controlled Sieverts manometric apparatus previously described elsewhere.[22] Sample temperature and gas pressure were recorded every 60 s using a K-type thermocouple (uncertainty of ± 1.5 °C) inserted directly into the sample and a digital pressure transducer (Rosemount 3051S) with a 0.035% span accuracy over 0 – 60 bar. During cycling of the $CaCO_3$-$CaTiO_3$

powder sample (~ 0.57 g) was loaded into a SiC sample cell (Saint-Gobain).[23] The sample cell was then placed under ~ 6 bar CO_2 back pressure to inhibit decomposition and heated at a ramp rate of 10 °C min^{-1} to 750 °C before the cycling was initiated. Desorption was carried out *in vacuo* for 1 h followed by absorption under initial $p(CO_2)$ = 5.45 bar for 2 h. The internal calibrated volumes were 38.22 cm^3 for the sample side volume, and 19.95 cm^3 for the reference volume. In total, 102 cycles were undertaken. The compressibility of CO_2 was obtained at each pressure and temperature from the NIST database 23 REFPROP (REference FLuid Properties).[24]

A Micromeritics TriStar II plus Surface Area & Porosity Analyser (Micromeritics, Norcross, GA, USA) was used to determine the specific surface area of the $CaCO_3$-$CaSiO_3$ and $CaCO_3$-$CaTiO_3$ samples before and after cycling, while and a Belsorp BelMini Surface Area & Porosity Analyser (Microtrac MRB, York, PA, USA) was used to analyse the $CaCO_3$-$CaZrO_3$ samples before and after cycling. The nitrogen (N_2) adsorption/desorption measurements were performed at 77 K. N_2 adsorption data, at relative pressures (p/p_0) between 0.05 and 0.30, were used to calculate the specific surface area by employing the Brunauer–Emmett–Teller (BET) multi-point method.[25]

Morphological images were collected by Scanning Electron Microscopy (SEM) using a Tescan Mira3 field emission microscope coupled with a secondary electron (SE) detector and integrated with an Oxford Instrument Energy Dispersive Spectroscopy (EDS) detector controlled by the Aztec software. The samples were prepared by dispersing powders on a carbon film upon an aluminium stub followed by sputter-coating with 3 nm of Pt. The images were collected using an accelerating voltage of 5 - 20 kV (for SEM images) and 20 kV (for EDS).

The levelised cost of electricity (LCOE) was calculated using equation (5), below:

$$LCOE = \frac{Sum\ of\ costs\ during\ plant\ lifetime}{Sum\ of\ electrical\ energy\ produced\ during\ plant\ lifetime} \quad (5)$$

The analysis assumed that the CO_2 produced in the decomposition of the prospective RCC is stored in a compressed state within a pressure vessel during the charging phase of the TCES system. The plant itself was assumed to be a 360-kWh system with 12 hours of storage and the main components of the plant were selected as a CO_2 compressor, intercoolers, turbines, an electrical heater system, heat exchanger, pressure and reactor vessels and a heat storage system. The costs accumulated during the lifetime of the plant can be classified as Capital Expenditure (CAPEX) or Operating Expenditure (OPEX).[26] The plant component costs were included as CAPEX and calculated using the constituent cost equations laid out by Couper *et al*.[26] The cost of $CaSiO_3$, $CaTiO_3$, and $CaZrO_3$ were also included as CAPEX for each use case. All costs are provided in US dollars. An analysis of 20- and 40-year useful plant lifetime was undertaken to understand the significance of an increased plant lifetime. Certain components were assumed to require replacement over a 40-year lifespan, such as the heat exchanger, CO_2 compressor, turbine, and heater, and these additional replacement costs were incorporated into the LCOE calculations for a 40-year plant lifetime use case.[27] The assumptions can be found in the ESI. OPEX costs include labour, service costs, along with annual operation and maintenance costs which were provided by the US National Renewable Energy Laboratory (NREL) System Advisor Model and adjusted for inflation every year, for both 20 and 40 years.[28] These fees were accumulated with the cost of the energy consumption for each component divided by the expected electrical energy output of a 360 kWh system running for 365 days a year for 20 and 40 years.

Results and discussion

$CaSiO_3$, $CaTiO_3$, and $CaZrO_3$ were synthesised and their composition confirmed by XRD data (Fig. 1(a), 2(a), and 3(a), respectively). Minor oxide traces of TiO_2 and ZrO_2 are observed in the respective $CaTiO_3$, and $CaZrO_3$ samples. The XRD data for the as-milled composites are shown in Fig. 1(b), 2(b), and 3(b) for $CaCO_3$-$CaSiO_3$, $CaCO_3$-$CaTiO_3$, and $CaCO_3$-$CaZrO_3$ respectively, indicating no reaction during milling. In addition, peaks for iron containing phases were not observed, concluding that the stainless steel vials and balls did not erode (to a limit above the limit of detection of XRD) due to the hardness of the metal oxide starting materials.

DSC-TGA data were collected for $CaCO_3$, and the ball-milled samples of $CaCO_3$-$CaSiO_3$, $CaCO_3$-$CaTiO_3$ and $CaCO_3$-$CaZrO_3$ to investigate the thermal decomposition properties of the mixtures compared with the parent compound (Fig. 4). The

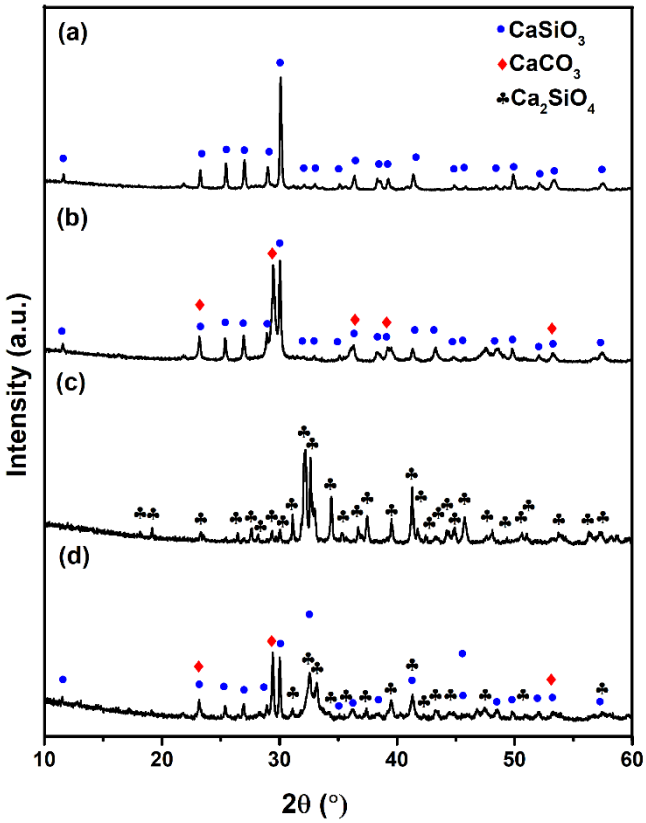

Fig. 1. XRD data of (a) synthesised $CaSiO_3$; (b) $CaCO_3$-$CaSiO_3$, ball-milled for 1h; (c) $CaCO_3$-$CaSiO_3$ after TGA up to 1200 °C and (d) $CaCO_3$-$CaSiO_3$ after 15 cycles at 750 °C (final stage: absorption). λ = Cu $K\alpha_{1,2}$ radiation.

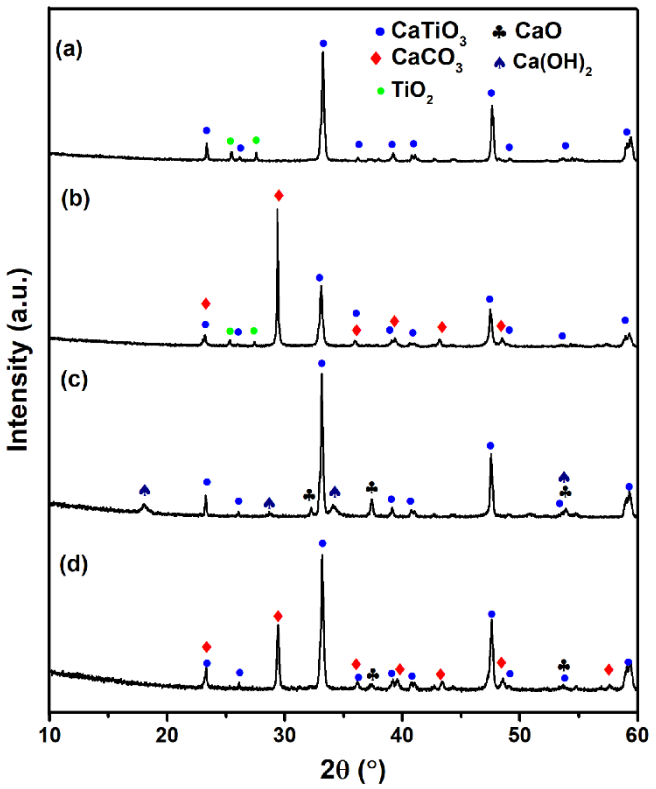

Fig. 2. XRD data of (a) synthesised $CaTiO_3$; (b) $CaCO_3$-$CaTiO_3$ ball-milled for 1h; (c) $CaCO_3$-$CaTiO_3$ after TGA up to 1200 °C and (d) $CaCO_3$-$CaTiO_3$ after 100 cycles at 750 °C (final stage: absorption). λ = Cu $K\alpha_{1,2}$ radiation.

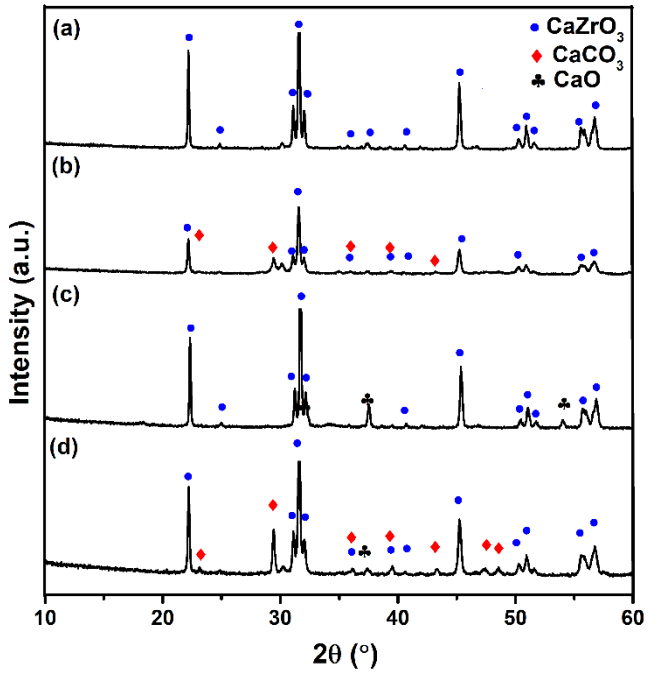

Fig. 3 XRD data of (a) synthesised $CaZrO_3$; (b) $CaCO_3$-$CaZrO_3$ ball-milled for 1h; (c) -$CaZrO_3$ after TGA up to 1200 °C and (d) $CaCO_3$-$CaZrO_3$ after 100 cycles at 750 °C (final stage: absorption). λ = Cu $K\alpha_{1,2}$ radiation.

addition of $CaSiO_3$, $CaTiO_3$ or $CaZrO_3$ to $CaCO_3$ decreases the decomposition temperature compared to pure $CaCO_3$, which indicates destabilisation of either the kinetics or

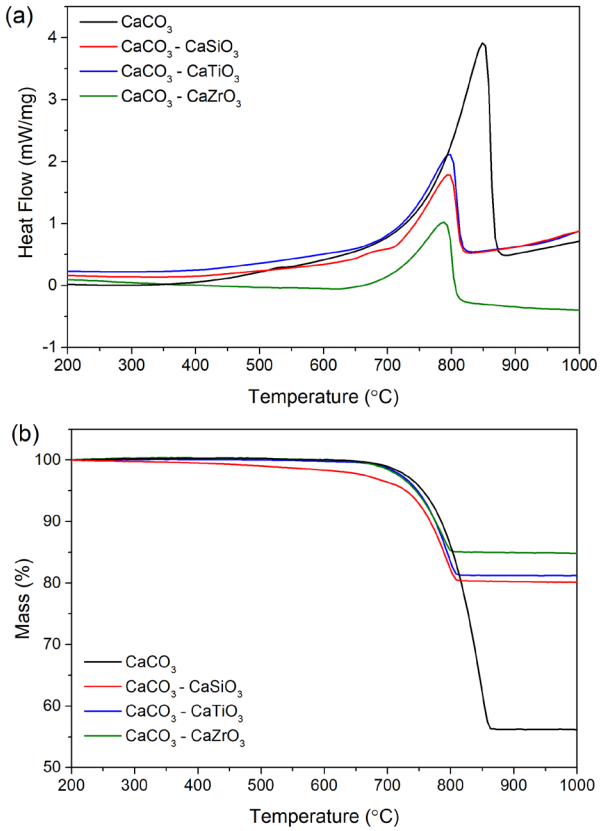

Fig. 4(a) DSC and (b) TGA data for $CaCO_3$, $CaCO_3$-$CaSiO_3$, $CaCO_3$-$CaTiO_3$, and $CaCO_3$-$CaZrO_3$.

Table 1 Measured enthalpy (ΔH_{des}) and CO_2 wt.% values from DSC/TGA measurements for $CaCO_3$, $CaCO_3$-$CaSiO_3$, $CaCO_3$-$CaTiO_3$, and $CaCO_3$-$CaZrO_3$.

	ΔH_{des} Measured and (theoretical) (kJ/mol CO_2)[19]	Measured and (calculated) CO_2 wt.%
$CaCO_{3(s)} \rightleftharpoons CaO_{(s)} + CO_{2(g)}$ (6)	176 ± 26 (165.7)	43.8 (44.0)
$CaCO_{3(s)} + CaSiO_{3(s)} \rightleftharpoons Ca_2SiO_{4(s)} + CO_{2(g)}$ (7)	111 ± 16 (121.3)	20.3 (20.3)
$CaCO_{3(s)} + CaTiO_{3(s)} \rightleftharpoons CaTiO_{3(s)} + CaO_{(s)} + CO_{2(g)}$ (8)	162 ± 24 (NA)	18.6 (18.6)
$CaCO_{3(s)} + CaZrO_{3(s)} \rightleftharpoons CaZrO_{3(s)} + CaO_{(s)} + CO_{2(g)}$ (9)	152 ± 22 (NA)	14.9 (15.7)

NA = not available; * Assuming ΔS_{des} = 143 J/mol/K (same as $CaCO_3$).

thermodynamics of CO_2 release from $CaCO_3$. Although decomposition commences at similar temperatures for each of the materials (~615 °C for $CaCO_3$; ~ 609 °C for $CaCO_3$-$CaSiO_3$; 586 °C for $CaCO_3$-$CaTiO_3$; 597 °C for $CaCO_3$-$CaZrO_3$), the maxima of the endothermic peaks (Fig. 4a) associated with CO_2 release were observed at significantly lower temperatures for the composites compared to pure $CaCO_3$ (850 °C for $CaCO_3$; 796 °C for $CaCO_3$-$CaSiO_3$; 797 °C for $CaCO_3$-$CaTiO_3$; 788 °C for $CaCO_3$-$CaZrO_3$). The measured weight loss for each composite was 43.8 % for $CaCO_3$, 20.3 % for $CaCO_3$-$CaSiO_3$, 18.6 % for $CaCO_3$-$CaTiO_3$, and 14.9 % for $CaCO_3$-$CaZrO_3$ (Fig. 4b), which corresponds to the

ARTICLE

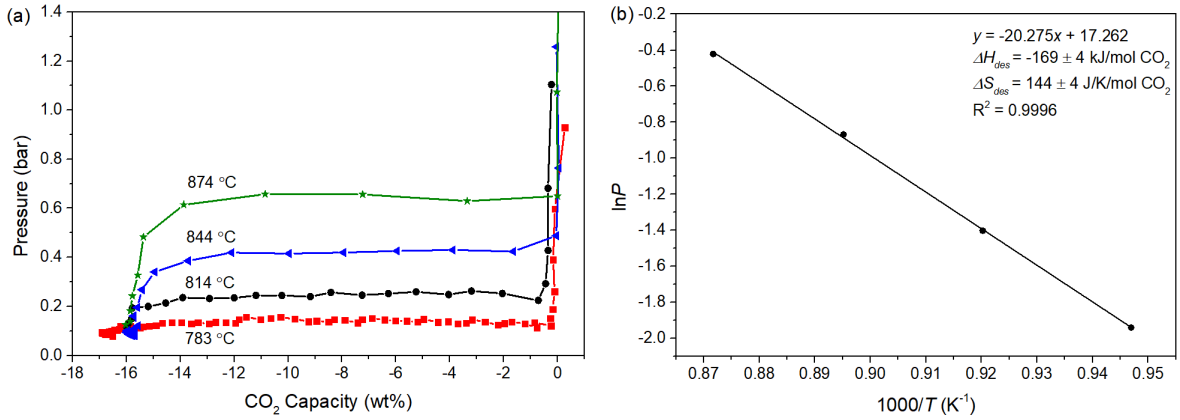

Figure 5. (a) Pressure-Composition-Isotherms (PCI) of $CaCO_3$-$CaTiO_3$ between 783 and 874 °C, and (b) corresponding van't Hoff plot.

expected theoretical CO_2 values according to eqs 6, 7, 8 and 9, respectively (Table 1).

The reaction enthalpy values (ΔH_{des}) for eqs 6 - 9, were determined by integrating the area of the CO_2 desorption peak in the DSC data and are summarised in Table 1. The ΔH_{des} of 176 ± 26 kJ/mol measured for $CaCO_3$ is consistent with the experimental value of 172 kJ/mol CO_2 from Pressure-Composition-Isotherms (PCI) and close to the theoretical value of 165.7 kJ/mol CO_2.[19, 29] Therefore, the decomposition enthalpy determined by DSC for each sample in this study is validated for quantitative comparison. The ΔH_{des} for the $CaCO_3$-$CaSiO_3$ system was measured to be 111 ± 16 kJ/mol CO_2, is close to the theoretical value of 120 kJ/mol CO_2 and verifies the theorised decomposition pathway to Ca_2SiO_4 (eqn. 7).[19] The measured ΔH_{des} for the $CaCO_3$-$CaTiO_3$ and $CaCO_3$-$CaZrO_3$ systems were determined as 162 ± 24 and 152 ± 22 kJ/mol CO_2, respectively. In summary, these results imply that addition of $CaSiO_3$ thermodynamically destabilises $CaCO_3$ as the $CaSiO_3$ takes part in the reaction and alters the decomposition reaction pathway of $CaCO_3$ reaction pathway, whereas addition of $CaTiO_3$ and $CaZrO_3$ alters the kinetics of the reaction as these materials are not altered during the reaction.

XRD data (Fig.1(c)) confirms that calcium orthosilicate (Ca_2SiO_4) is the solid decomposition product from the $CaCO_3$-$CaSiO_3$ system as shown in eqn (7). There are no reports in the literature for the formation Ca_2TiO_4 or Ca_2ZrO_4, with both being assumed to be unstable and it is unclear why these phases cannot be synthesised.[18–20] As such the decomposition products for $CaCO_3$-$CaTiO_3$ and $CaCO_3$-$CaZrO_3$ are CaO and $CaTiO_3$, and CaO and $CaZrO_3$, respectively (Figs 2(c) and 3(c)). Peaks for $Ca(OH)_2$ are visible in the diffraction pattern for $CaCO_3$-$CaTiO_3$ but this is due to the reaction of CaO with moisture after the high temperature experiment was undertaken.

As the $CaCO_3$-$CaTiO_3$ system has shown favourable thermal analysis results through DSC-TGA, the thermodynamics of desorption were accurately determined for this system using PCI analysis. The equilibrium pressure of desorption was measured at four temperatures ranging from 783 to 874 °C, with the results illustrated in Fig. 5(a). The CO_2 capacity corroborated the TGA results with ~16 wt.% being determined using the Sieverts' apparatus. A van't Hoff plot determined ΔH_{des} = 169 ± 4 kJ/mol CO_2 and ΔS_{des} = 144 ± 4 J/K/mol CO_2, with an associated R^2 of 0.9996 (Fig 5(b)). These values provide two vital pieces of information. First, it supports that the enthalpy of reaction determined by DSC of 162 ± 24 kJ/mol CO_2. Second, it supports the assumption that the reaction pathway follows Eq. 8, in that the sorption that occurs is the reversible formation of CaO and $CaCO_3$, rather than Ca_2TiO_4. Recently, ΔH_{des} = 172 ± 8 kJ/mol CO_2 and ΔS_{des} = 146 ± 7 J/K/mol CO_2 was determined for pure $CaCO_3$ by PCI analysis, which is almost identical to the value determined here for the $CaCO_3$-$CaTiO_3$ system. Therefore the 1 bar operating temperature for this system, $T_{des(1\ bar\ CO2)}$, using a ΔH_{des} = 169 ± 4 kJ/mol CO_2 and ΔS_{des} = 144 ± 4 J/K/mol CO_2 is 901 ± 33 °C.

Determination of the sorption thermodynamics and conditions for each sample allowed for CO_2 cycling using TGA under an alternating inert and CO_2 atmosphere. For the $CaCO_3$-$CaSiO_3$ and $CaCO_3$-$CaTiO_3$ samples, the initial cycling evaluation was achieved by heating to 900 °C at 20 °C/min under an Ar flow to initiate CO_2 desorption, followed by cooling to 500 °C (Fig. S1). Then a CO_2 flow (0.8 bar partial pressure) was applied with a heating ramp (10 °C/min) from 500 to 900 °C. This experiment showed that in the limited time (17.5 minutes) $CaCO_3$-$CaSiO_3$ absorbed 7 wt.% CO_2 compared to the 16.5 wt.% CO_2 initially desorbed from the sample, while $CaCO_3$-$CaTiO_3$ absorbed 10 wt.% compared to the 18.6 wt.% CO_2 initially desorbed. $CaCO_3$-

$CaZrO_3$ was also cycled under similar conditions although a maximum temperature of 1000 °C was employed during the initial decomposition (Fig. S2). This sample showed an initial mass loss of 15 wt.% followed by a slightly limited absorption of 12.5 wt.%. The low amount of absorption seen in the samples is a consequence of both thermodynamics and kinetics. Thermodynamic constraints cause CO_2 absorption to cease when the sample temperature reaches the point where a 0.8 bar equilibrium pressure limit exists, as dictated by thermodynamics. This is exemplified by using the thermodynamics measured by PCT for $CaCO_3$-$CaTiO_3$ (ΔH_{des} = 169 ± 4 kJ/mol CO_2 and ΔS_{des} = 144 ± 4 J/K/mol CO_2) which gives a 0.8 bar operating temperature of 886 °C which is just lower than the 900 °C maximum temperature employed during desorption during TGA cycling. Temperature dependent kinetic limitations may limit the CO_2 absorption within the allocated timeframe. Nevertheless, these experiments show that cycling is possible under TGA conditions at particular pressures and temperatures.

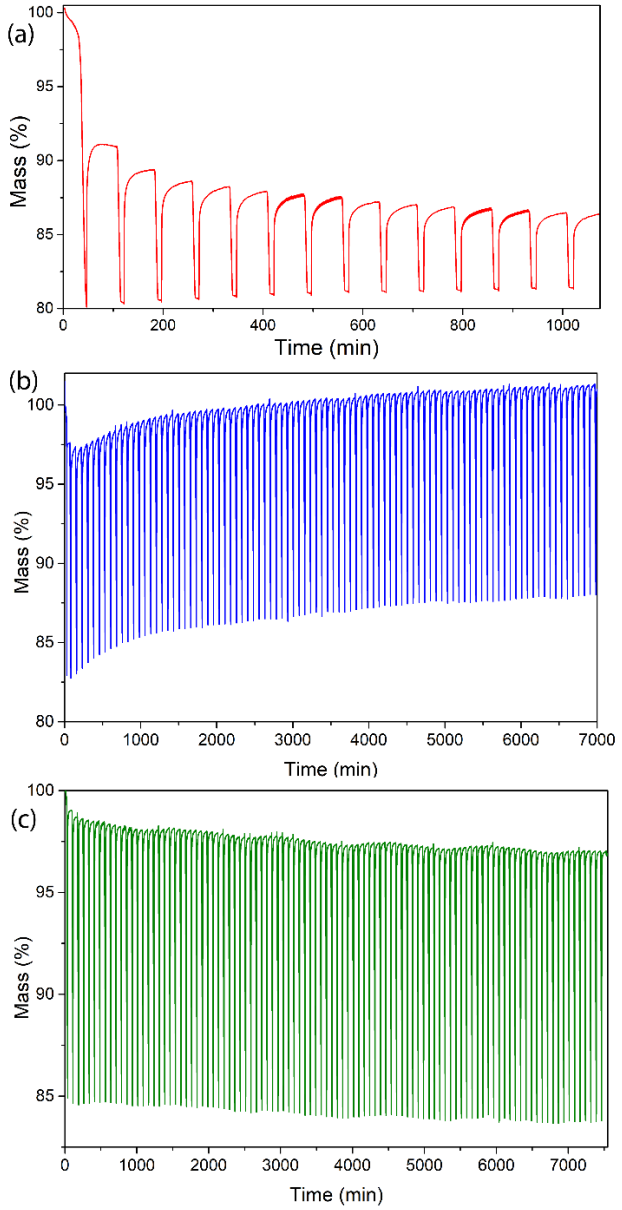

Fig. 6. CO_2 desorption and absorption cycles for (a) $CaCO_3$-$CaSiO_3$ (14 cycles), (b) $CaCO_3$-$CaTiO_3$ (100 cycles), and (c) $CaCO_3$-$CaZrO_3$ (100 cycles) at 750 °C as measured by TGA. Desorption was carried out under Ar flow, while absorption was carried out under CO_2 flow (0.8 bar partial pressure). Absorption time steps = 60 min, desorption = 15 mins.

Table 2 Quantitative composition of the crystalline components (wt.%) provided from X-ray diffraction-based Rietveld analysis on CO_2 cycled material (final stage: absorption). Mathematical fitting uncertainties are provided in parentheses. The Rietveld refinement plots are illustrated in Figs. S4 – S6 in the ESI.

Material (Space group number)	$CaCO_3$-$CaSiO_3$ after cycling (wt.%)	$CaCO_3$-$CaTiO_3$ after cycling (wt.%)	$CaCO_3$-$CaZrO_3$ after cycling (wt.%)
$CaCO_3$ (167)	16.1(3)	30.8(3)	29.2(3)
CaO (225)	2.2(1)	1.14(8)	-
$CaSiO_3$ (14)	25.1(4)	-	-
Ca_2SiO_4 (62)	46.6(5)	-	-
$Ca_5(SiO_4)_2CO_3$ (14)	10.1(4)		
$CaTiO_3$ (62)	-	68.0(3)	-
$CaZrO_3$ (62)	-	-	67.8(3)
ZrO_2 (137)	-	-	3.0(2)

The CO_2 cycling in the TGA was then carried out at a constant temperature of 750 °C, using CO_2 (or argon) gas flow to control sorption (Fig. 6). Desorption was carried out under an Ar flow, while absorption was carried out under a mixture of Ar and CO_2 flow (0.8 bar CO_2 partial pressure). $CaCO_3$-$CaSiO_3$ presents a CO_2 conversion rate of approximately 56 wt.% of the theoretical maximum capacity of 20 wt.% during the first cycle, which decreases to 33 wt.% over 14 cycles (Fig. 4). Ca_2SiO_4 was previously reported as a CO_2 absorbent at 500 – 800 °C with a maximum capacity of 45.7 %, which is consistent with the result found in this study.[30] A decrease in the cyclic capacity of TCES materials such as $CaCO_3$ has previously been attributed to changes in morphology, agglomeration and particle growth,[14] but the presence of 10.1(4) wt.% $Ca_5(SiO_4)_2CO_3$ was also observed in the sample by XRD (Fig. 1(d) and Table 2). This material will potentially continue to form over time, reducing the available $CaCO_3$ and $CaSiO_3$ that can undergo reversible carbonation. In addition to $Ca_5(SiO_4)_2CO_3$, quantitative XRD analysis (Table 2) also showed that after cycling 16.1(3) wt.% $CaCO_3$, 25.1(4) wt.% $CaSiO_3$, 46.6(5) wt.% Ca_2SiO_4 was contained in the sample, along with 2.2(1) wt.% CaO. BET analysis was undertaken to determine if the loss of CO_2 capacity was indeed attributed to a decrease in specific surface area (Table 3). Before cycling, the specific surface area for $CaCO_3$-$CaSiO_3$ was 15.32 ± 0.03 $m^2\ g^{-1}$ and after 14 cycles this decreased by 46% to 8.21 ± 0.08 $m^2\ g^{-1}$. Loss of specific surface area is a common problem observed by carbonates during multiple cycles of CO_2 desorption and absorption at high temperatures.[14]

In contrast to the $CaCO_3$-$CaSiO_3$ system, $CaCO_3$-$CaTiO_3$ desorbed 17.1 wt.% CO_2 on the first cycle and reabsorbed 14.7 wt.% CO_2 which is 72 % of its theoretical capacity of 18.7 wt.% (Fig 6(b)). Subsequently, the next 99 cycles showed consistent capacity with a final absorption of 71 % of the theoretical capacity, which

Table 3. Structural properties of $CaCO_3$-$CaSiO_3$, $CaCO_3$-$CaTiO_3$, and $CaCO_3$-$CaZrO_3$ before and after cycling as determined by BET analysis.

	Specific surface area (m^2 g^{-1})
$CaCO_3$-$CaSiO_3$	15.32 ± 0.03
$CaCO_3$-$CaSiO_3$ after 14 cycles	8.21 ± 0.08
$CaCO_3$-$CaTiO_3$	18.32 ± 0.11
$CaCO_3$-$CaTiO_3$ after 100 cycles	17.73 ± 0.09
$CaCO_3$-$CaZrO_3$	9.4 ± 1.5
$CaCO_3$-$CaZrO_3$ after 100 cycles	2.6 ± 1.5

is a total loss of 5% of its overall capacity. After cycling, XRD was had occurred that would reduce the cyclic capacity (Fig. 2(d) and Table 2). After cycling, the material has a specific surface area of 17.73 ± 0.09 m^2 g^{-1}, which represents a difference of approximately 3 % compared to the value of the ball-milled material, 18.32 ± 0.11 m^2 g^{-1} (Table 3). This indicates that significant sintering of the particles did not occur during the cycling and explains the strong cyclic CO_2 capacity.

In a similar fashion, $CaCO_3$-$CaZrO_3$ shows a first cycle CO_2 conversion rate of 90 % of the maximum value of 15.7 wt.%, decreasing to 84 % and remaining stable over 100 cycles (Fig. 6(c)). Quantitative XRD analysis of the cycled material showed only 29.2(3) wt% $CaCO_3$, 67.8(3) wt% $CaZrO_3$ and 3.0(2) wt% ZrO_2 (Fig. 3(d) and Table 2). The latter of which accounts for some of the cyclic capacity loss, especially if it is formed as a crust on the outside of the particles. It should be reiterated that the impressive results shown by the $CaCO_3$-$CaTiO_3$ and $CaCO_3$-$CaZrO_3$ systems are not due to reactive carbonate composites, but instead $CaCO_3$ with Ca*M*O_3 additives (*M* = Ti/Zr), which are loaded in a 1:1 molar ratio. This high level of cyclic stability shows great promise for technical applications, despite the high level of additive addition of 57.6 and 64.2 wt.% for $CaTiO_3$ and $CaZrO_3$, respectively.

Further CO_2 cycling was also performed on $CaCO_3$-$CaTiO_3$ at 752 °C with a manometric Sieverts apparatus under 5.45 bar for absorption (Figure S3). This technique employed a larger sample size of 0.54 g (compared to mg-scale in the TGA) and higher CO_2 absorption pressures aiming to better represent the thermodynamic and cyclic stability/energy capacity under conditions relevant to potential industrial operations.[31] It was found that cycling with 2 h absorption steps allowed for ~ 83 % CO_2 storage capacity consistently over 102 cycles. This capacity corroborates the cycling performed at the same temperature using TGA. The absorption kinetics were relatively fast and the reaction was completed in ~ 300 s.

BET analysis of each of the samples investigated by TGA indicated that the specific surface area for the $CaCO_3$-$CaSiO_3$ and $CaCO_3$-$CaZrO_3$ samples was reduced upon cycling, while $CaCO_3$-$CaTiO_3$ remained relatively unchanged. Morphological studies using SEM and EDS analyses were undertaken to assess the cause of the reduction in surface area. As can be seen from Fig. 7, the loss of specific surface area for $CaCO_3$-$CaSiO_3$ after cycling was caused by increased particle size (from sub-micron to micron-scale) after cycling, which is indicative of sintering and agglomeration. The EDS results show a homogeneous distribution of Ca (orange), O (green), and Si (purple) before and after the cycles, indicating that $CaCO_3$, $CaSiO_3$, and Ca_2SiO_4 have a similar morphology and continue to be distributed homogeneously through the sample. This homogeneity is expected considering that all elements participate in the reversible reactions within the reactive carbonate composite. The analysis of $CaCO_3$-$CaTiO_3$ samples before and after cycling (Fig. 8) shows contrasting behaviour when compared with $CaCO_3$-$CaSiO_3$ (Fig. 7). After cycling, through EDS, it is possible to observe sub-micron particles of $CaTiO_3$ among the $CaO/CaCO_3$ particles that appear to have agglomerated into

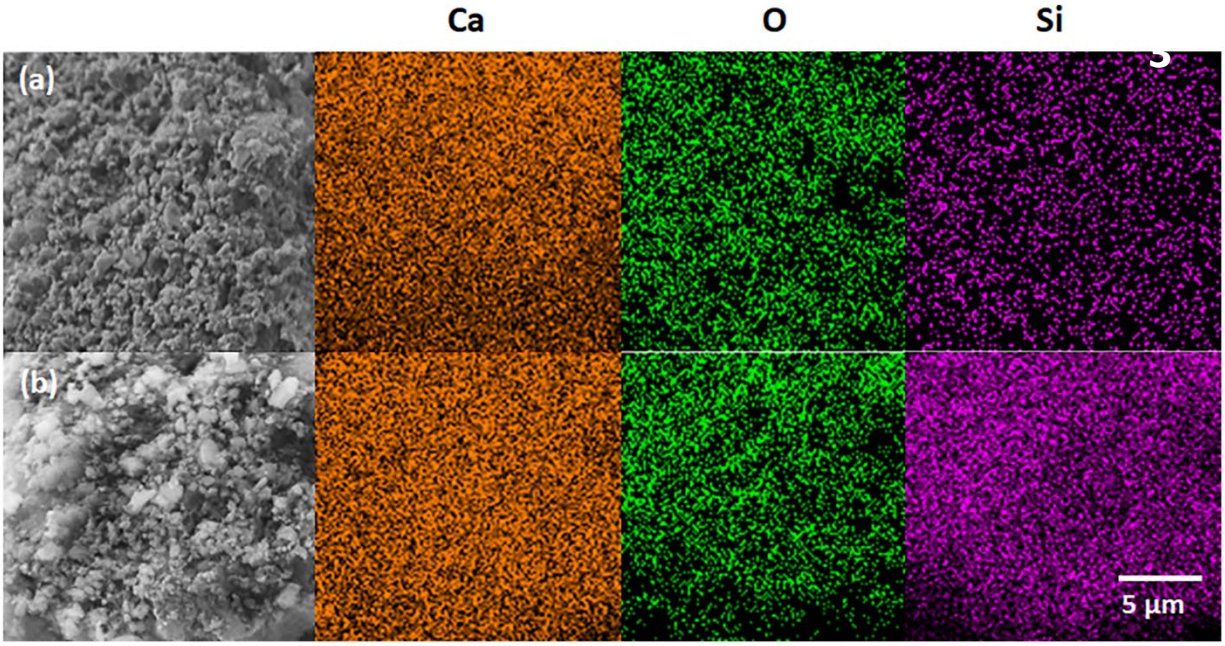

Fig. 7 SEM and EDS mapping of the $CaCO_3$-$CaSiO_3$ (a) before and (b) after CO_2 cycling (14 cycles, final stage: absorption) BSE mode, 20 kV.

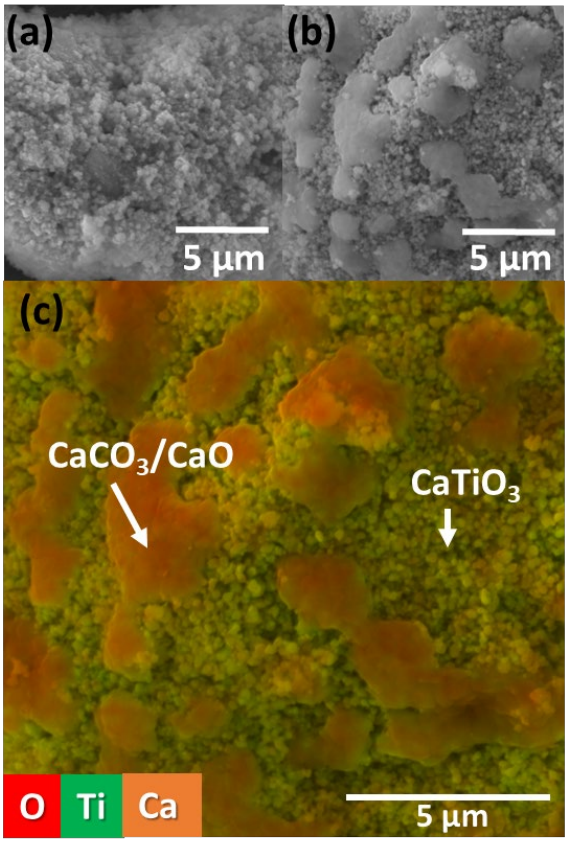

Fig. 8 SEM and EDS mapping of the $CaCO_3$-$CaTiO_3$ (a) before and (b and c) after CO_2 cycling. BSE mode, 20 kV.

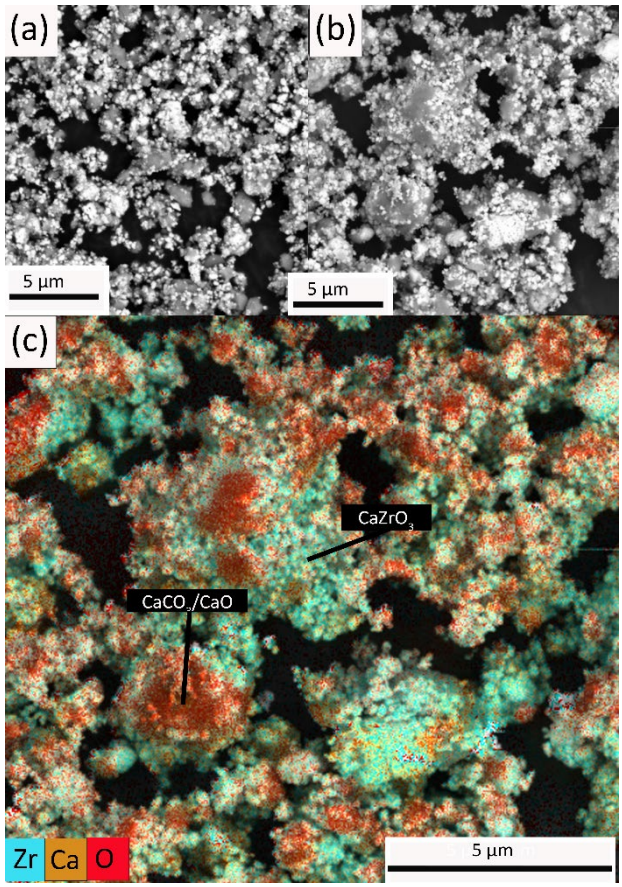

Fig. 9 SEM and EDS mapping of the $CaCO_3$-$CaZrO_3$ (a) before and (b and c) after CO_2 cycling. BSE mode, 20 kV.

larger multi-micron scale particles (Figs. 8(b) and 8(c)). These results show that $CaTiO_3$ particles have resistance to sintering at high temperature. Furthermore, $CaTiO_3$ acts as a spacer between $CaCO_3$/CaO particles, restricting further agglomeration of these particles and consequently keeping the CO_2 cycling process stable. Similarly, SEM and EDS of $CaCO_3$-$CaZrO_3$ samples before and after cycling also showed that the particles of $CaZrO_3$ remain at a constant size during cycling at high temperature, while the $CaCO_3$/CaO particles again increase in size (Fig. 9). As seen with $CaCO_3$-$CaTiO_3$, the $CaCO_3$-$CaZrO_3$ particles act as spacers to avoid further agglomeration during cycling.

Among the samples investigated, $CaCO_3$-$CaSiO_3$ presents a significant loss of cyclic CO_2 capacity in the first few cycles due to sintering at 750 °C, however, $CaCO_3$-$CaTiO_3$ and $CaCO_3$-$CaZrO_3$, have shown great stability of 83 and 84 % respectively, and high kinetic performance over absorption/desorption cycles at 750 °C. In Table 4 and Fig. S1 (ESI) there is a comparison between different carbonate systems based on calcium, strontium, and barium that have been investigated for TCES and compared with commercial molten salt ($40NaNO_3$:$60KNO_3$), which is the material used in the current technology for TES.

Each of the carbonate derivatives listed in Table 4 presents a higher gravimetric and volumetric energy density than molten salt, which means that less space is required to store the same amount of energy. The cost of energy storage was then calculated for each of the materials. Despite the cyclic capacity and energy density possessed by the $CaCO_3$-$CaTiO_3$ and $CaCO_3$-$CaZrO_3$ systems, the high materials cost of TiO_2 ($2,200 USD/mt (metric ton)) and ZrO_2 ($4,464 USD/mt) will inevitably prevent these systems from being employed rather than molten salts which cost $630 USD/mt.[32, 33] One option to reduce to costs is to reduce the quantity of $CaTiO_3$ or $CaZrO_3$ to less than 1:1 ratio. The $CaCO_3$-$CaSiO_3$ system is 41 % cheaper than the molten salt mixture but additional materials costs may take effect if an anti-agglomeration additive is identified to assist its cyclic capacity. For instance, $SrCO_3$-$SrSiO_3$, and $BaCO_3$-$BaSiO_3$ reactive composites also require the use of catalysts to improve their reaction kinetics and cyclic stability.[10, 11] Recently, a system

Table 4 Comparison of thermochemical properties, system variables, and cost parameters for select energy storage materials. A more extensive data set is provided in Table S1 (ESI).[10, 11, 14, 32, 33]

	ΔH (kJ kg^{-1})[a]	Operating Temperature (°C)	Operating CO_2 Pressure (bar)	Mass Required (tonnes)[b]	Materials Cost (US$ tonne^{-1})	Material cost (US$ per kWh_{th})
Molten salt (40$NaNO_3$:60KNO_3)	413	290 - 565	-	11.6	630	5.7
$SrCO_3$ + $SrSiO_3$	500	700	0.1 - 6.0	5.8	1,060	7.6
$BaCO_3$ + $BaSiO_3$	309	850	5 - 25	8.7	1,090	12.7
$CaCO_3$ + 20 wt% Al_2O_3	782	900	1	3.4	84.3	0.4
$CaCO_3$ + $CaSiO_3$	513[c]	750	0.1 - 1	5.5	260	1.8
$CaCO_3$ + $CaTiO_3$	716[d]	750	0.1 - 1	4.0	2200	11.1
$CaCO_3$ + $CaZrO_3$	544[c]	750	0.1 - 1	5.2	4664	30.9

[a]Per kg of total material; [b]To generate 360 kWh of electrical energy. [c]This work, DSC data. [d]This work, PCI data. Assuming 100 % cycling capacity, except $CaCO_3 \rightleftharpoons CaO+CO_2$ (20 wt% Al_2O_3) which assumes 45.7 % as in ref. [14].

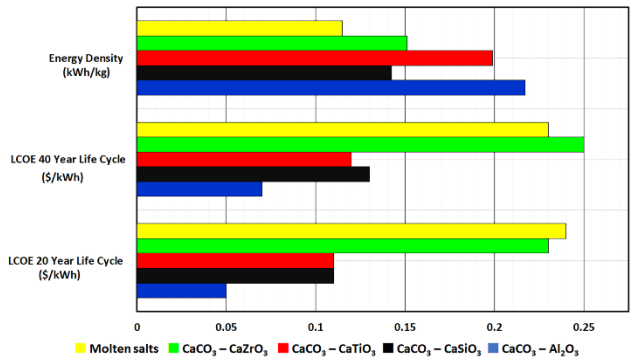

Fig. 10 Levelised cost of electricity (LCOE) for 20 and 40 year cycle life and energy density comparison for $CaCO_3$-$CaZrO_3$, $CaCO_3$-$CaTiO_3$, $CaCO_3$-$CaSiO_3$ and $CaCO_3$-Al_2O_3. Costs are in USD. Assumptions for calculations are in the ESI. LCOE for Molten Salts are based on a 100 MW system[34], while the LCOEs determined for the materials in this study are for a 360 kW system.

using $CaCO_3$-Al_2O_3 as a starting material for TCES at 900 ºC was presented highlighting its high cyclic capacity retention (80 - 90 %) and inexpensive cost.[14] $CaCO_3$-Al_2O_3 has a lower material cost of $84 USD/mt leading to a materials cost of $0.4 USD/$kWh_{th}$ compared with $CaCO_3$-$CaSiO_3$ ($1.8 USD/$kWh_{th}$), $CaCO_3$-$CaTiO_3$ ($11 USD/$kWh_{th}$) and $CaCO_3$-$CaZrO_3$ ($31 USD/$kWh_{th}$), however, the entire system cost also needs to be taken into account, since operating at lower temperatures (750 °C rather than 900 °C) could allow for a less expensive containment system.

For commercial uptake of thermal batteries, the cost of the materials is important but more crucial is the levelised cost of electricity (LCOE). The LCOE was calculated for the $CaCO_3$-$CaSiO_3$, $CaCO_3$-$CaTiO_3$, $CaCO_3$-$CaZrO_3$, and $CaCO_3$-Al_2O_3 materials for a 360 kWh energy storage system (12 h storage), coupled to a Stirling engine for electricity production, assuming an input cost of electricity of $0.10 USD/kWh and a wholesale capital cost of PV electricity as $750/kW (see ESI for further assumptions).[35, 36] The CO_2 system is also a closed circuit, where the CO_2 desorbed is collected and used for absorption. As can be seen in Fig. 10, the systems using $CaCO_3$-Al_2O_3, $CaCO_3$-$CaSiO_3$, $CaCO_3$-$CaTiO_3$ and $CaCO_3$-$CaZrO_3$ have a LCOE of 0.05, 0.11, 0.11 and 0.23 $/kWh, respectively, for a 40-year life cycle and 0.07, 0.13, 0.12 and 0.25 $/kWh, respectively, for a 20-year life cycle. Each of these LCOE's, apart from the $CaCO_3$-$CaZrO_3$ system is cheaper than the LCOE determined for molten salts that is the current state-of-the art. This cost analysis includes the price of solar PV within the CAPEX costs, alongside the individual mechanical systems required for the plant and the initial investment of the plant. The operational costs include the price of energy storage material, as well and service and maintenance costs. Both capital and operational costs are adjusted year on year for inflation. These values are comparable with the techno-economic comparison of energy storage reported in the literature, which highlights that for a 100 MW wind-PV hybrid power system, the LCOE of energy storage would be 0.1224, 0.1812, 0.1863 and 0.2225 USD/kWh for TES, battery, hydrogen storage, and pumped hydro storage, respectively.[37] Although there are order of magnitude differences between the material cost for calcium carbonate derivatives, the difference in LCOE using $CaCO_3$-Al_2O_3, $CaCO_3$-$CaTiO_3$, and $CaCO_3$-$CaZrO_3$ are less than a factor of two, which makes $CaCO_3$-$CaTiO_3$ and $CaCO_3$-$CaZrO_3$ potentially competitive materials for TCES given their outstanding performance at 750 °C.

Conclusions

This study has demonstrated that metal carbonates such as $CaCO_3$ show potential as TCES materials for thermal battery applications. Compared to the current molten salt state-of-the-art TES materials, $CaCO_3$ (with additives) has a greater volumetric and gravimetric energy density meaning less weight and volume of material is required to store the same amount of energy. Particle agglomeration currently hinders $CaCO_3$ as a TES material, although additives have been shown to alleviate this issue. This study has demonstrated the potential for $CaSiO_3$, $CaTiO_3$ and $CaZrO_3$ to be added to $CaCO_3$ to increase the cyclic efficiency of the material and gain commercial application. Despite the high cost of $CaCO_3$-$CaTiO_3$ and $CaCO_3$-$CaZrO_3$ of \$11.1 and 30.9 USD/kWh_{th}, these materials demonstrated excellent cyclic performance with a sustained capacity of 83 and 84%, respectively, at 750 °C.

The $CaCO_3$-$CaSiO_3$ system was cost effective at \$1.8 USD/kWh_{th} but showed a significant efficiency loss of 66 wt% over 14 cycles under 1 bar CO_2 at 750 °C. SEM imaging and BET analysis of the $CaCO_3$-$CaSiO_3$ material showed that major particle agglomeration had occurred for this material but not for $CaCO_3$-$CaTiO_3$ and $CaCO_3$-$CaZrO_3$. The latter materials act as particle refinement agents and do not directly react with the $CaCO_3$ powder, whereas $CaCO_3$-$CaSiO_3$ react to form CaO and Ca_2SiO_4. The addition of a particle refinement agent to $CaCO_3$-$CaSiO_3$ may increase its cyclability, but at the detriment of energy density and cost. Despite the costs of the materials being relatively high, determination of the LCOE over 20 and 40 years has shown that once the cost of the required infrastructure is included, the costs of the materials are similar with a range of 0.39 – 0.59 USD/kWh for a 20 year LCOE.

Author Contributions

All authors have approved the final version of the manuscript.

Conflicts of interest

There are no conflicts to declare.

Acknowledgements

CEB, MP, TDH and EM acknowledge the Department of Industry, Science, Energy and Resources for funding from a 2019 Global Innovation Linkage (GIL73589) grant Round 2. CEB, MP, TDH, APV and YL acknowledge the financial support of the Australian Research Council for ARC Discovery grant DP200102301.

Notes and references

1 D. Abbott, *Proc. IEEE*, 2010, **98**, 42-66.
2 D. N. Harries, M. Paskevicius, D. A. Sheppard, T. E. C. Price and C. E. Buckley, *Proc. IEEE*, 2012, **100**, 539-549.
3 D. A. Sheppard, M. Paskevicius, T. D. Humphries, M. Felderhoff, G. Capurso, J. Bellosta von Colbe, M. Dornheim, T. Klassen, P. A. Ward, J. A. Teprovich, C. Corgnale, R. Zidan, D. M. Grant and C. E. Buckley, *Appl. Phys. A*, 2016, **122**, 395.
4 L. Desage, E. McCabe, A. P. Vieira, T. D. Humphries, M. Paskevicius and C. E. Buckley, *Journal of Energy Storage*, 2023, **71**, 107901.
5 T. Bauer, W.D Steinmann, D. Laing and R. Tamme, in *Annual Review of Heat Transfer* Stuttgart 2005, vol. 15, pp. 131-177.
6 M. Adams, C. E. Buckley, M. Busch, R. Bunzel, M. Felderhoff, T. W. Heo, T. D. Humphries, T. R. Jensen, J. Klug, K. H. Klug, K. T. Møller, M. Paskevicius, S. Peil, K. Peinecke, D. A. Sheppard, A. D. Stuart, R. Urbanczyk, F. Wang, G. S. Walker, B. C. Wood, D. Weiss and D. M. Grant, *Progress in Energy*, 2022, **4**, 032008.
7 M. Liu, N. H. S. Tay, S. Bell, M. Belusko, R. Jacob, G. Will, W. Saman and F. Bruno, *Renew Sust Energ Rev*, 2016, **53**, 1411-1432.
8 A. J. Carrillo, J. González-Aguilar, M. Romero and J. M. Coronado, *Chem. Rev.*, 2019, **119**, 4777-4816.
9 F. Raganati and P. Ammendola, *Energy Fuels*, 2023, **37**, 1777-1808.
10 A. P. Vieira, K. Williamson, T. D. Humphries, M. Paskevicius and C. E. Buckley, *J. Mater. Chem. A*, 2021, **9**, 20585-20594.
11 K. T. Møller, K. Williamson, C. E. Buckley and M. Paskevicius, *J. Mater. Chem. A*, 2020, **8**, 10935-10942.
12 K. Williamson, K. T. Møller, A. M. D'Angelo, T. D. Humphries, M. Paskevicius and C. E. Buckley, *Phys. Chem. Chem. Phys.*, 2023, **25**, 7268-7277.
13 K. Williamson, Y. Liu, T. D. Humphries, A. M. D'Angelo, M. Paskevicius and C. E. Buckley, *Energy*, 2024, Submitted.
14 K. T. Møller, A. Ibrahim, C. E. Buckley and M. Paskevicius, *J. Mater. Chem. A*, 2020, **8**, 9646-9653.
15 A. Mathew, N. Nadim, T. T. Chandratilleke, M. Paskevicius, T. D. Humphries and C. E. Buckley, *Solar Energy*, 2022, **241**, 262-274.
16 K. T. Møller, A. Berger, M. Paskevicius and C. E. Buckley, *J. Alloys Compd.*, 2022, **891**, 161954.
17 K. T. Møller, T. D. Humphries, A. Berger, M. Paskevicius and C. E. Buckley, *Chemical Engineering Journal Advances*, 2021, **8**, 100168.
18 K. Manickam, P. Mistry, G. Walker, D. Grant, C. E. Buckley, T. D. Humphries, M. Paskevicius, T. Jensen, R. Albert, K. Peinecke and M. Felderhoff, *Int. J. Hydrogen Energy*, 2019, **44**, 7738-7745.
19 M. Outotec, HSC Chemistry Software 9, https://www.mogroup.com/portfolio/hsc-chemistry/, (accessed January 10, 2023).
20 Y. Osamu, Y. Kazuhide, T. Kiyoshi and S. Kiyoshi, *Chem. Lett.*, 1979, **8**, 401-404.
21 R. A. Young and R. A. Young, *The Rietveld Method*, Oxford University Press, 1995.
22 M. Paskevicius, D. A. Sheppard and C. E. Buckley, *J. Am. Chem. Soc.*, 2010, **132**, 5077-5083.
23 D. A. Sheppard, M. Paskevicius, P. Javadian, I. J. Davies and C. E. Buckley, *J. Alloys Compd.*, 2019, **787**, 1225-1237.
24 E. W. Lemmon, I. H. Bell, M. L. Huber and M. O. McLinden, *NIST Standard Reference Database 23: Reference Fluid Thermodynamic and Transport Properties*, Gaithersburg, 2018.
25 S. Brunauer, P. H. Emmett and E. Teller, *J. Am. Chem. Soc.*, 1938, **60**, 309-319.
26 J. R. Couper, W. R. Penney, J. R. Fair and S. M. Walas, in *Chemical Process Equipment (Third Edition)*, eds. J. R. Couper, W. R. Penney, J. R. Fair and S. M. Walas, Butterworth-Heinemann, Boston, 2012, DOI: https://doi.org/10.1016/B978-0-12-396959-0.00021-5, pp. 731-741.
27 G. Towler and R. Sinnott, in *Chemical Engineering Design (Second Edition)*, eds. G. Towler and R. Sinnott, Butterworth-Heinemann, Boston, 2013, DOI:

https://doi.org/10.1016/B978-0-08-096659-5.00007-9, pp. 307-354.
28 N. Blair, N. DiOrio, J. Freeman, P. Gilman, S. Janzou, T. Neises and M. Wagner, *System Advisor Model (SAM) General Description (Version 2017.9.5) NREL/TP-6A20-70414*, National Renewable Energy Laboratory, 2018.
29 L. Desage, T. D. Humphries, M. Paskevicius and C. E. Buckley, *Journal of Energy Storage*, 2024, Submitted: DOI: 10.2139/ssrn.4561027.
30 M. Wang, C.-G. Lee and C.-K. Ryu, *Int. J. Hydrogen Energy*, 2008, **33**, 6368-6372.
31 A. Bayon, R. Bader, M. Jafarian, L. Fedunik-Hofman, Y. Sun, J. Hinkley, S. Miller and W. Lipiński, *Energy*, 2018, **149**, 473-484.
32 Metals Prices, https://www.metal.com/, (accessed December 11, 2023).
33 T. D. Humphries, K. T. Møller, W. D. A. Rickard, M. V. Sofianos, S. Liu, C. E. Buckley and M. Paskevicius, *J. Mater. Chem. A*, 2019, **7**, 1206-1215.
34 A. Boretti and S. Castelletto, *Journal of Energy Storage*, 2021, **42**, 103143.
35 Australian Energy Regulator - Industry Charts, https://www.aer.gov.au/industry/wholesale/charts, (accessed December 20, 2023).
36 SOLARQUOTES AUSTRALIAN SOLAR PRICE INDEX, https://www.solarquotes.com.au/price-explorer/, (accessed March 06, 2024).
37 Y. He, S. Guo, J. Zhou, F. Wu, J. Huang and H. Pei, *Energy Conv. Manag.*, 2021, **229**, 113779.